

On-Chip Rolling Design for Controllable Strain Engineering and Enhanced Photon–Phonon Interaction in Graphene

Lu Wang, Ziao Tian, Biran Zhang, Borui Xu, Tianbo Wang, Yang Wang, Shilong Li, Zengfeng Di,* and YongFeng Mei*

On-chip strain engineering is highly demanded in 2D materials as an effective route for tuning their extraordinary properties and integrating consistent functionalities toward various applications. Herein, rolling technique is proposed for strain engineering in monolayer graphene grown on a germanium substrate, where compressive or tensile strain could be acquired, depending on the designed layer stressors. Unusual compressive strains up to 0.30% are achieved in the rolled-up graphene tubular structures. The subsequent phonon hardening under compressive loading is observed through strain-induced Raman G band splitting, while distinct blueshifts of characteristic peaks (G^+ , G^- , or 2D) can be well regulated on an asymmetric tubular structure with a strain variation. In addition, due to the strong confinement of the local electromagnetic field under 3D tubular geometry, the photon–phonon interaction is highly strengthened, and thus, the Raman scattering of graphene in rolled-up tubes is enhanced. Such an on-chip rolling approach leads to a superior strain tuning method in 2D materials and could improve their light–matter interaction in a tubular configuration, which may hold great capability in 2D materials integration for on-chip applications such as in mechanics, electronics, and photonics.

1. Introduction

Graphene has attracted intense attention due to its unique properties and potential applications arising from its 2D hexagonal lattice structure with an atomic-level thickness and high

L. Wang, B. R. Zhang, B. R. Xu, Y. Wang, Prof. Y. F. Mei
Department of Materials Science and State Key
Laboratory of ASIC and System
Fudan University
Shanghai 200433, P. R. China
E-mail: yfm@fudan.edu.cn

Prof. Z. A. Tian, T. B. Wang, Prof. Z. F. Di
State Key Laboratory of Functional Materials for Informatics
Shanghai Institute of Microsystem and Information Technology
Chinese Academy of Sciences
Shanghai 200050, P. R. China
E-mail: zfdi@mail.sim.ac.cn

Dr. S. L. Li
State Key Laboratory of Infrared Physics
Shanghai Institute of Technical Physics
Chinese Academy of Sciences
Shanghai 200083, P. R. China

 The ORCID identification number(s) for the author(s) of this article can be found under <https://doi.org/10.1002/sml.201805477>.

DOI: 10.1002/sml.201805477

specific surface area.^[1,2] The nontrivial band structure of graphene near the Fermi level enables a series of appealing phenomena, e.g., the anomalous quantum Hall effect,^[3] ultrahigh electron mobility,^[4] and superior thermal conductivity,^[5] rendering it a promising candidate for the next generation of micro/nanoelectronic devices. With respect to its current status and future perspectives, it is of great significance to fully explore the tunability of the properties of graphene by various methods, e.g., doping,^[6] gating,^[7] and strain engineering.^[8,9] Among these approaches, strain engineering is capable of altering the lattice symmetry of graphene, thus tuning its electronic band structure,^[10,11] which could be superior in the bandgap opening,^[12] conductance modulation,^[13,14] and the formation of strong magnetic field.^[15]

For a realistic graphene-integrated optoelectronic device in an on-chip manner, such as optical modulators,^[16] silicon–graphene photodetectors,^[17,18] and broadband polarizer,^[19] strain engineering is desired in order to provide a flexible approach for tuning the electrical structure of graphene. However, developed strain-tuning methods, such as the deformation of flexible substrates,^[20,21] piezoelectric substrate actuation,^[22] and pressurized blisters,^[23] are hardly compatible with on-chip applications. Particularly, using the rolling method as a reliable approach for both optimal yields and effective strain manipulation^[24–26] suggests direct and precise tuning with target morphologies and thus their mechanical properties.^[27] Based on rolling geometry, the corresponding strain states in graphene can be designed and accurately realized, as summarized in **Figure 1**, where the tensile strain in graphene could be introduced through the transfer process of graphene onto conventional semiconductors.^[28,29] However, compressive strain in graphene is seldom reported because the critical compressive strain for buckling is several orders of magnitude smaller than the critical tensile strain for fracturing.^[30] Furthermore, for a few compressive strain cases, it is essential to explore the fundamental physics of out-of-plane deformation, which often occurs during the compression process.

On the other hand, the innovative 3D architecture based on 2D graphene and graphene oxide enables morphology-engineered performance, such as strong mechanical properties,

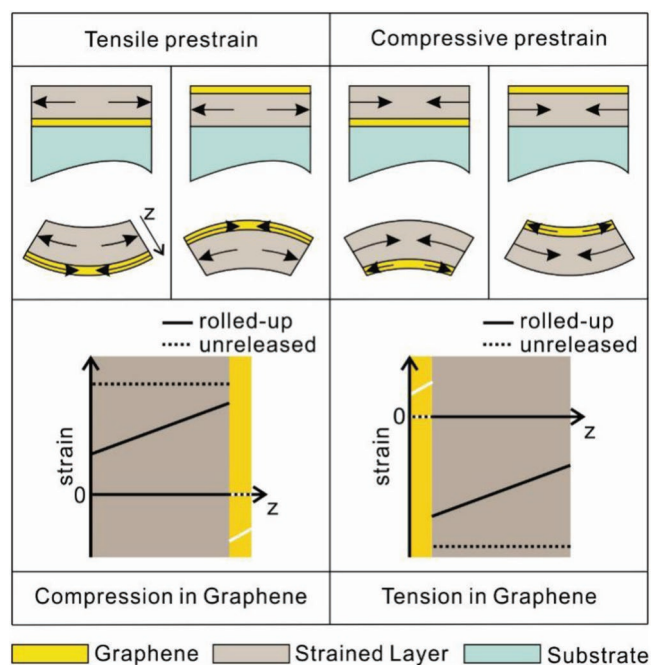


Figure 1. Strategies for strain engineering in rolled-up graphene. The phenomena can be concluded into two cases of tensile or compressive prestrain, which results in compression or tension in rolled-up graphene, respectively. The arrow depicts the strain direction. The diagrams in the lower panel quantitatively describe the strain state across the thickness of nanomembrane, where the z -axis is the radial direction from the inner to the outer side.

high effective surface area, and fast transport kinetics.^[31,32] Developing 3D blocks has been proposed as an effective approach for the morphology tuning of 2D units, which can be referred to foams, templates, and aerogels.^[33–35] In the rolled-up 3D tubular configuration, the achieved nanoscale confinement of the electromagnetic field could greatly enhance the photon–phonon interaction, thus realizing enhanced Raman scattering.^[36] Such an enhanced Raman scattering characteristic is supposed to be a novel principle for light–matter interaction, which is free from the intrinsically high Ohmic losses when applying the traditional method used for metal.^[37] This property should also enhance the coupling of the evanescent field between the graphene layer and tubular structure, which could alleviate the problem of a low signal-to-noise ratio, thus inspiring novel constructions for potential applications of graphene-based optical devices.^[38] Moreover, rolling technique could offer an approach to the 3D configuration of graphene and other 2D materials for the controllable on-chip strain engineering and boosted phonon–photon interaction that lab-in-a-tube systems^[39–41] rely on, which include a wide range of functionalities such as optical microcavities,^[42,43] photodetectors,^[44] actuators,^[45,46] and micromotors.^[47]

In this study, we propose a general route for constructing graphene/ Y_2O_3/ZrO_2 microtubes based on chemical vapor deposition (CVD)-grown monolayer graphene through rolled-up technology for strain engineering with a transfer-free advantage. As depicted in Figure 1, compressive strain is introduced in graphene as designed to be the first case (the z -axis depicts the radial direction from the inner to the outer side), where the

exact magnitude of the strain is further illustrated by solving the equilibrium strain state. Since strain would modify the graphene phonon frequency, it is demonstrated through Raman measurements that the doubly degenerate Raman G band would split into two singlet bands, G^+ and G^- . Additionally, the Raman G^+ , G^- , and 2D bands exhibit significant blueshifts with an increasing magnitude of the compressive strain observed on a tapered microtube. Polarized Raman spectroscopy further validates the distinctive polarization dependence of the G^+ and G^- bands, which allows us to determine the crystallographic orientation of graphene. Moreover, the strongly confined electromagnetic field of the 3D tubular structure makes a contribution to the increased Raman intensity, demonstrating future perspectives on light–matter interactions. In general, our work not only technically provides a method for introducing a sufficient strain for on-chip devices but also fulfills a comprehensive study on phonon physics of graphene under compressive loads and inspires the scheme for greatly enhanced light–matter coupling. Moreover, rolling technique can also provide a platform for achieving tension in graphene or other 2D materials, as illustrated in the right panel of the compressive prestrain states in Figure 1, where the resultant magnitude of the strain can be engineered. The target performance of materials, which is responsive to the mechanical behavior of either compression or tension, can be precisely and effectively implemented based on the rolling method.

2. Results and Discussion

2.1. Fabrication of Rolled-up Graphene

The graphene oxide microtubes are fabricated through a rolled-up technique, as depicted in Figure 2a, which involves both the top-down and bottom-up approaches. A trilayer nanomembrane is deposited and patterned based on the top-down process. Combined with the bottom-up approach, the patterned nanomembranes could be constructed into tubular structures after being released from the substrate. Through CVD techniques, the homogeneous monolayer graphene was grown on a Ge (110) wafer.^[48,49] Generally, it was supposed that the single-crystal graphene was grown on hydrogen (H)-terminated Ge surface, implying the van der Waals interaction between graphene and substrate.^[50] Actually, the interaction is much more complex during the growth. Since the commercially available Ge substrate consists of flat terraces separated by atomic steps, the formation of strong chemical bonding between graphene and the step exists, as reported in our previous work.^[51] As the merging of graphene islands under increasing deposition time, a complete single-crystal graphene layer forms, attaching to the substrate via van der Waals force instead of chemical bonding (see Part S1 in the Supporting Information). Through the chemical etching of the Ge underlayer, the interaction would be broken, thus releasing the monolayer graphene and enabling the rolling process as the experimental design. To characterize the quality of as-grown graphene, the high-resolution C 1s X-ray photoelectron spectroscopy (XPS) spectrum of graphene is shown in Figure 2b. It is clear that the dominated peak is located at 284.8 eV, which is originated

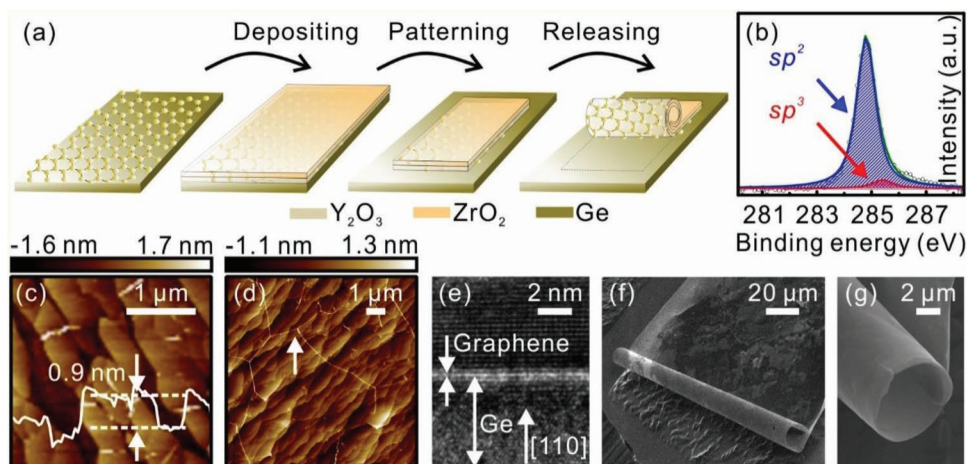


Figure 2. Fabrication and characteristics of the graphene oxide microtube. a) Schematics of the nanofabrication process using rolled-up technology. The transparent bilayer stands for the deposited Y_2O_3 and ZrO_2 using light yellow and light orange, respectively. b) XPS spectrum of CVD-grown graphene. c) AFM image with high magnification of graphene with partial coverage on the Ge wafer. The white line depicts the height difference. d) AFM image with low magnification of graphene with full coverage on Ge wafer. e) STEM image of the cross-section of graphene with full coverage on the Ge wafer. f) SEM image and g) an enlarged view of the rolled-up graphene oxide microtube on the Ge wafer.

from the nonfunctionalized sp^2 carbon atoms. The insignificant peak at 285.4 eV is aliphatic sp^3 carbon atoms due to natural contamination in air, which indicates the purity of the corresponding CVD-grown graphene.^[35,52] Figure 2c shows an atomic force microscopy (AFM) image with high magnification of the graphene with partial coverage on a Ge wafer, which is obtained under deposition time of 180 min. It is demonstrated that a uniform height difference of 0.9 nm exists between the graphene and Ge substrate, which suggests that the graphene is monolayer. The AFM image with low magnification of graphene with partial coverage on Ge wafer gives a distinct view of the single-crystal graphene islands, which is shown in Figure S2 in the Supporting Information. By increasing the growth time to 240 min, monolayer graphene with full coverage on Ge wafer would be prepared. As a consequence of intact graphene layer on Ge substrate, the height difference in single-crystal Ge dominates the color distribution in the AFM image, as shown in Figure 2d. The wrinkle in monolayer graphene, as depicted by the white arrow, happens during the cooling procedure due to the difference of thermal expansion between graphene and Ge underlayer. For the 3D microtube, those wrinkles are considered to make no difference. The AFM image with low magnification exactly indicates the integrity of as-grown graphene, which experimentally meets following demands. The growth of graphene with full coverage on Ge substrate is further validated by cross-sectional scanning transmission electron microscopy (STEM), as exhibited in Figure 2e.

Afterward, 10 nm Y_2O_3 and 30 nm ZrO_2 layers were deposited onto graphene through electron beam evaporation to achieve the prestrain state for the rolling process.^[53] Then, photolithography and ion beam etching were adopted to pattern the graphene oxides layered structure. The oxide bilayer would roll up into microtubes with the adhesion of graphene on the outer surface once released from the substrate by etching the sacrificial layer of Ge with the heated H_2O_2 solution (40% concentration). Some details of the trilayer morphology during the formation of microtubes can be found in Part S1 in the

Supporting Information. Figure 2f exhibits the scanning electron microscopy (SEM) image of the rolled-up structure on the Ge with a tilt angle, which reveals its 3D architecture. Additionally, the rough surface on the exposed Ge substrate is due to the anisotropic etching process. The inhomogeneity in the brightness of the microtube is believed to be attributed to the uneven electron accumulation. Through the enlarged view in Figure 2g, it can be clearly seen that a stereoscopic construction with a radius of $\approx 4 \mu\text{m}$ is composed of the rolled-up nanomembrane with excellent smoothness. The statistical radius distribution is shown in Figure S4 in the Supporting Information, indicating good uniformity and reliability. Thus, the rolled-up graphene oxide microtube with an external radius of $\approx 4 \mu\text{m}$ and a wall thickness of 40 nm is fabricated as expected.

2.2. Raman Scattering in a Tubular Geometry

To experimentally monitor the enhanced electromagnetic field and mechanical response of rolled-up graphene, micro-Raman measurements working under the double resonance process is employed to provide effective information on the optical and geometrical properties.^[54] Figure 3a shows the Raman spectra of as-grown, released, and rolled-up graphene under an excitation laser wavelength of 514 nm. It should be noted that the thermal heating effect is evaluated by performing a series of Raman measurements under different laser powers, as shown in Figure S5 in the Supporting Information. Graphene has features three Raman peaks, i.e., the D band, G band, and 2D band. The G peak usually comes from the doubly degenerate E_{2g} phonon at the Brillouin zone center, and the 2D peak, as the overtone of the D peak, is believed to originate from the intervalley scattering of two phonons with opposite wavevectors. As shown in Figure 3a, the “disorder” D peak is imperceptible for the as-grown graphene, which indicates the high quality of pristine graphene layer without defects. Generally, it is of practical significance to preserve the intrinsic structure

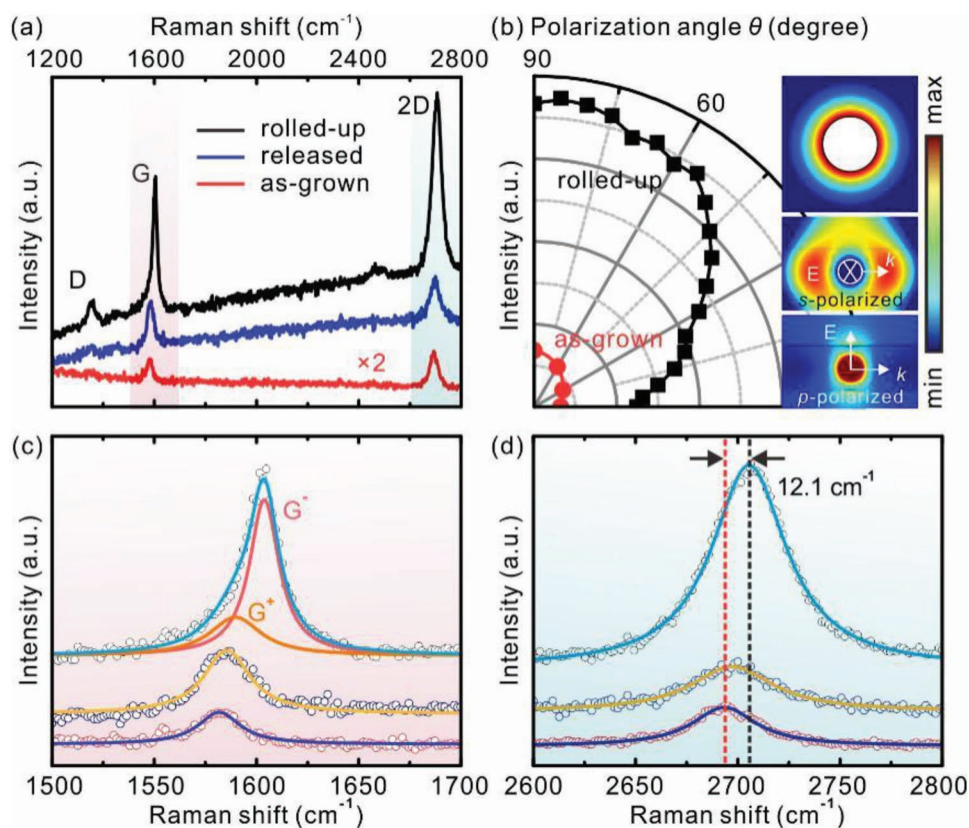


Figure 3. Characterization of enhanced Raman scattering, and strain-induced band splitting and blueshift. a) Raman spectra for the as-grown (red), the released but unrolled (blue), and the rolled-up graphene (black). The spectrum of the as-grown graphene is given by multiplying the original data by 2. b) Intensity distribution of the 2D bands in polar coordinates. The insets are the electromagnetic field for the cross-section and the enlarged part with incident light polarization. Enlarged views of c) the G bands (the pink region in (a)) and d) the 2D bands (the blue region in (a)) through Lorentz fitting. The orange and red lines stand for the fitting results for the G⁺ and G⁻ peaks in (c), respectively. The fitting results are dark blue, yellow, and light blue for the as-grown, the released, and the rolled-up graphene, respectively.

of pristine graphene in experiments. After the rolled-up process, the defect-related D peak starts to emerge (1350 cm⁻¹), while the bandwidths of both the G and 2D peaks are almost unchanged. Thus, the slightly enhanced intensity of the D peak can be mainly attributed to the enhanced Raman intensity based on the 3D structure. Additionally, it is assumed that few defects induced in the experimental process would not destroy the quality and integrity of the graphene layer, which could still meet the demand of essential experimental aspects.

Moreover, the intensity of the Raman signal for the released graphene is higher than the as-grown one, which can be attributed to the decrease in the substrate effect since the nanomembrane is nearly suspended on the substrate. Most importantly, it is observed that the Raman signal is highly enhanced as the outermost layer of graphene is integrated with microtubes, which is dominated by the electromagnetic field of the tubular structure. The intensity distributions of the 2D band for as-grown (red) and rolled-up (black) graphene further validate the enhanced Raman characteristics, as shown in Figure 3b. The electromagnetic field distribution around the microtube is calculated by the finite-difference time-domain (FDTD) method (see Part S3 in the Supporting Information), which attests to increased coupling with graphene, as shown in the upper inset of Figure 3b. Additionally, the electromagnetic field distributions with the

polarized light parallel and perpendicular to the graphene layer (middle and down insets, respectively) suggest polarization-dependent characteristics of the electromagnetic field, and the simulation results match well with the experimental intensity variations, which are attributed to the anisotropic absorption of graphene.^[19] From the s-polarized scattering measurement (polarization state parallel respective to the graphene layer), it is observed that the resultant maximum value is obtained at $\theta = 90^\circ$ (θ is the angle from the perpendicular to parallel orientation with respect to the tube axis). Such an enhancement of the electromagnetic field could be unusual in the enhanced Raman performance, so it has potential in promoting the application in a field that involves light-matter interaction.^[55]

Meanwhile, both G and 2D peaks are quite sensitive to the presence of strain. It is demonstrated that the Raman frequency of graphene on the microtube structure is strongly influenced, thus leading to the splitting of the G peak and a blueshift of the 2D peak, as depicted in the enlarged view of the Raman spectra in Figure 3c. The G band splits into two bands with parallel (G⁻) and perpendicular (G⁺) orientation with respect to the strain axis, where the Lorentz fitting results provide a clear and straight view of the G⁺ and G⁻ peaks located at 1589.7 and 1603.8 cm⁻¹, respectively. In comparison, the G peak position is located at 1581.8 cm⁻¹ for the planar graphene. While

no splitting of the 2D peak is observed due to the insufficient strain magnitude, the 2D peak position shifts from 2693.4 to 2705.5 cm^{-1} , leading to a 12.1 cm^{-1} blueshift, as shown in Figure 3d. The Raman peaks stay almost the same for both the as-grown and released graphene, which suggests that no in-plane strain is introduced during the release process, as the released graphene without rolling has an infinite radius. In addition, the distinct blueshifts of the Raman peaks indicate the compressive strain has been generated on the rolled-up graphene, which is further verified through the following strain-engineering model.

2.3. Modeling of Strain Distribution

Recently, several approaches have been proposed to build a platform for rolled-up graphene with conventional semiconductors through the transfer process of graphene, where graphene acts as the inner layer of the rolled-up structure.^[28,29,56] However, the interactions of the transferred graphene with additional materials strongly vary among different studies, which appear to be either tensile^[28,29] or strain-free.^[56] In our case, the in-plane strain state redistribution for the nontransfer rolled-up graphene oxides structure with a high reproducibility is studied and illuminated. The initial state of the graphene layer is set as $\epsilon_0(\text{Gr}) = 0$ for the convenience of comparison with the resultant strain state. The difference in the strain values between the Y_2O_3 and ZrO_2 layer is near 0.93%, which is obtained by solving the equation according to the measured radius of the rolled-up microtube, calculated as^[57]

$$\text{Radius} = \frac{Y_1' t_1^4 + Y_2' t_2^4 + 2Y_1' Y_2' t_1 t_2 (2t_1^2 + 2t_2^2 + 3t_1 t_2)}{6Y_1' Y_2' t_1 t_2 (t_1 + t_2) (\eta_1 \epsilon_1^0 - \eta_2 \epsilon_2^0)} \quad (1)$$

The parameters used above include thickness t_i , Young's modulus Y_i , Poisson's ratio ν_i , and initial strain ϵ_i^0 of the layer i . Additionally, $Y_i' = \frac{Y_i}{1 - \nu_i^2}$, and $\eta_i = 1 + \nu_i$ as we defined (see Table S1 in the Supporting Information). As a consequence of the predominant strain states, the graphene/ Y_2O_3 / ZrO_2 trilayer structure rolls upward with the graphene at the outermost as depicted in Figure 4a, where the t and l axes are on behalf of the tangential and longitudinal components of the in-plane direction and the z -axis is on behalf of the radial direction. Figure 4b depicts the rolled-up InGaAs/GaAs/graphene structure, which is proposed in ref. [29]. For the tensile prestrain state in the graphene/ Y_2O_3 / ZrO_2 trilayer structure, we suppose the strain in the Y_2O_3 layer is near 0 and the ZrO_2 layer is near 0.93%. When releasing the membranes, the elastic relaxation occurs, which results in a redistribution of the strain. The total strain energy in a trilayer construction is obtained by integrating the strain energy density over the layer thickness (t_i), as^[58]

$$U_{\text{total}} = \sum_{i=1}^3 \int_0^{t_i} \frac{Y_i'}{\nu_i'^2 + 1} (\epsilon_i^2 + \epsilon_i'^2 + 2\nu_i' \epsilon_i^i \epsilon_i^i) dz \quad (2)$$

where ϵ_i^i is the transverse component of the in-plane strain and the longitudinal component $\epsilon_i^l = 0$ in our case. By solving the equilibrium strain state for the curved film, the in-plane strain across the trilayer is obtained (see Part S4 in the Supporting Information). The strains in the as-grown (ϵ_0) and rolled-up

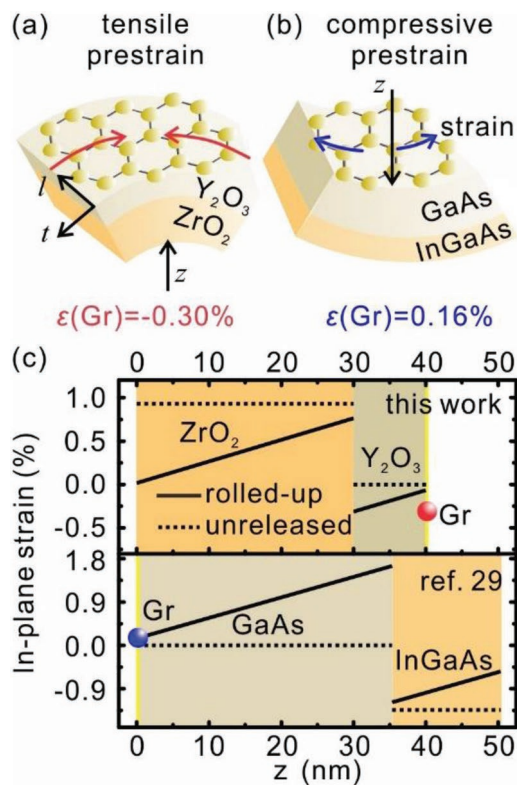


Figure 4. Modeling the strain distribution in rolled-up microstructure. a) Schematic of an enlarged part for the rolled-up graphene/ Y_2O_3 / ZrO_2 structure's cross-section. The t and l axes are on behalf of the tangential and longitudinal components of the in-plane direction, while the z -axis is on behalf of the radial direction. b) Schematic of the rolled-up InGaAs/GaAs/graphene structure. c) The calculated strain across the z -axis from the inner to the external surface (solid line) based on a graphene/ Y_2O_3 / ZrO_2 microtube with a radius of 4 μm (upper panel) and the InGaAs/GaAs/graphene microtube in ref. [29] (lower panel). The dashed lines present the initial strain before the releasing process. The resultant strains in the rolled-up graphene are depicted by circles. Gr refers to graphene.

trilayer structure (ϵ_i) are plotted in the upper panel of Figure 4c, where the z -axis is from the inner to the external surface in the radial direction. As expected, the tensile strain in the ZrO_2 layer increases from the inner surface to the interface, while the Y_2O_3 layer experiences a compressive strain, which decreases from the interface to the external side. The resultant strain redistribution across the layer's thickness further supports our assumption of the initial strain state for the oxide bilayer based on the model. In particular, the magnitude of strain in the rolled-up graphene is calculated as $\epsilon(\text{Gr}) = -0.30\%$ for a microtube with a radius of 4 μm (highlighted as the red ball in Figure 4c). The negative value indicates the compressive strain in graphene, which matches well with the strain state deduced from Raman measurements. We also analyzed the strain states of the InGaAs/GaAs/graphene microtube in ref. [29], which can be classified as case 4 in Figure 1. According to the InGaAs/GaAs/graphene structure exhibited in Figure 4b, the resultant strain in graphene is calculated to be 0.16%, as shown in the lower panel of Figure 4c (blue ball). The positive value means the tension in graphene as the inner layer, which also agrees with our model and validates its feasibility.

2.4. Strain Analysis on an Asymmetric Tube

Despite the nearly perfect demonstrated tubular structure, there are asymmetric microtubes with gradual variations in radius, which are achieved due to the uneven rolling process. The microscopy image of a tapered graphene oxide microtube is shown in Figure S6a in the Supporting Information, on which the Raman mapping tests are performed following the path as depicted using green dots. Hence, we further explore the relationship among the Raman shift, compressive strain, and radius. Figure 5a exhibits the mapping results for the microtube with a decreased radius from 7.5 to 3.4 μm . As expected, the G and 2D peaks are identified through distinct color distributions, and distinct blueshifts occur as the diameter decreases. While the G^+ and G^- peaks cannot be resolved from the mapping results, two individual bands are analyzed and clearly exhibited after Lorentz fitting in Figure 5b. The magnitudes of the shifts for the three bands vary from one another, yielding a 3, 8, and 12 cm^{-1} shift for the G^+ , G^- , and 2D bands, respectively. We can conclude that the blueshifts for the 2D band are relatively larger than that for the G^+ band, which matches with previous reports.^[21] By considering the strain distributed along an asymmetric tubular structure with a variable radius, the relationship between the strain and radius can be obtained by solving the equilibrium strain state (see Figure S6b in the Supporting Information). Both the geometric solution and calculation data suggest that the relationship between the

strain and radius nearly follow $\varepsilon \propto 1/R$. Figure 5c exhibits the regular shift behavior of the G^+ , G^- , and 2D bands under the gradually increased strain. With a strain magnitude less than 0.22%, we can obtain the shift rates of -17 ± 4.5 , -81 ± 7.9 , and $-156 \pm 17.7 \text{ cm}^{-1} \text{ \%}^{-1}$ for the G^+ , G^- , and 2D bands, respectively, through the linear fitting results. The resultant considerable slopes indicate that the effective strain is introduced to the graphene, while the deviation may be deduced from other force effects, such as shear strain, which was omitted in our simplified model. In particular, it has been demonstrated that a nonlinear trend for the Raman shift with strain occurred (marked as the gray region), since the detachment between the graphene and the oxide layer may gradually arise, especially when loading a large compressive strain. Hence, the initial slope is constant and high, while the subsequent plateau is captured at large strains using the polynomial fitting method. Consequently, the out-of-plane deformation of graphene under a high compressive strain and weak constraint is achieved and supposedly strongly influences its electronic properties, which demands a more detailed study in the future.^[59,60]

2.5. Graphene Crystallographic Orientation on Rolls

Moreover, in order to demonstrate the splitting of the G peak, the direction of the polarization is varied for the rolled-up graphene under a fixed strain state ($\approx 0.16\%$). The monolayer

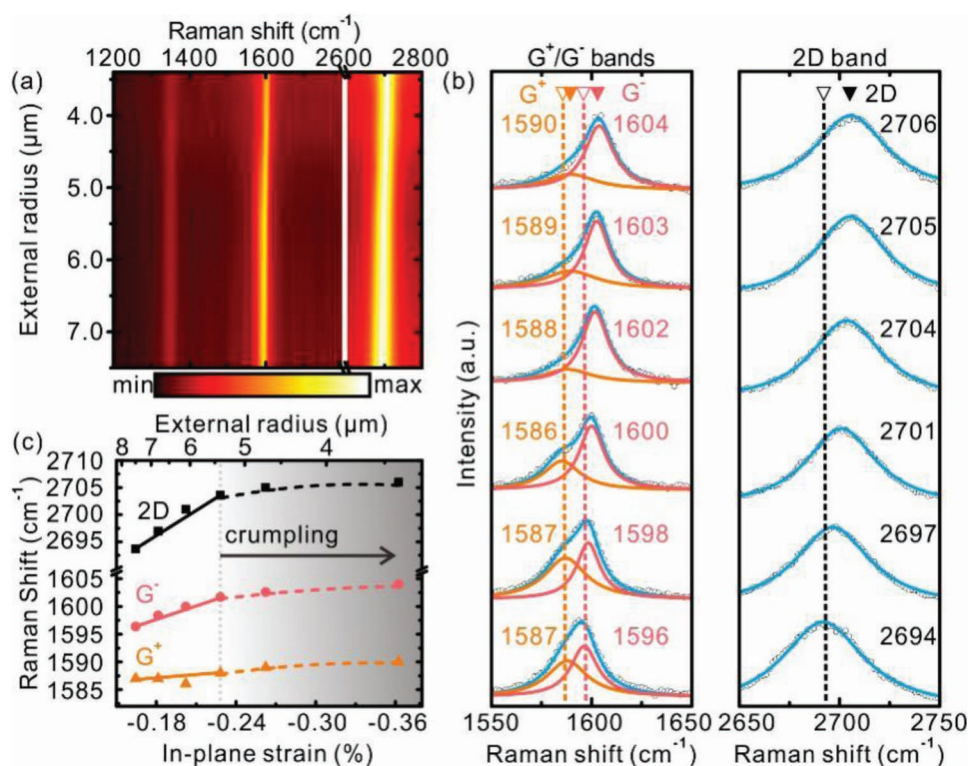


Figure 5. Raman measurements and strain analysis on an asymmetric microtube. a) Raman mapping of a microtube with a gradually decreasing external radius. b) Lorentz fitting results for the data extracted from (a). The dashed lines, together with hollow triangles, are presented as a reference for the peak positions of the large radius, and the solid triangles are for the small radius. c) The relationship between the Raman shift and the calculated strain of the tapered microtube. The solid lines are the fitting results from the peak positions using the linear fitting method. In the gray region, the dashed curves are the fitting results using the polynomial fitting method, where crumpling occurs with increasing strain.

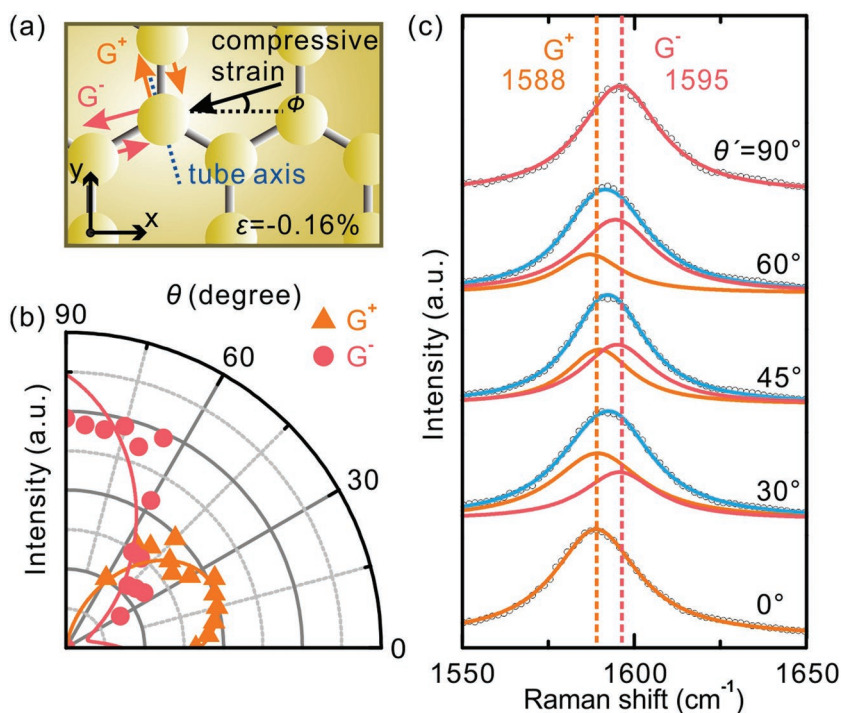


Figure 6. Polarization dependence of the doubly degenerate G band. a) Schematic of monolayer graphene under compressive strain. The eigenvectors of the G^+ and G^- bands polarized perpendicularly and parallel to the strain axis, respectively. The x -axis denotes the graphene crystallographic orientation. b) Intensity distribution in the polar coordinates and c) Raman spectra of the fitted G^+ and G^- bands under polarized Raman measurements. The data are fitted to $I_{G^+} \propto \cos^2(\theta_{\text{out}} - 20^\circ)$ and $I_{G^-} \propto \sin^2(\theta_{\text{out}} - 20^\circ)$ in (b). θ' is defined as $\theta - 20^\circ$ in (c).

graphene under compressive strain and the resultant splitting of the G band are schematically exhibited in **Figure 6a**. In general, we define ϕ as the direction for the strain axis from the graphene crystallographic x -axis, since the graphene is not aligned symmetrically along the tube axis, which would induce an indefinite orientation of the phonon eigenvectors. As illustrated in ref. [20], the intensity of the G^+ and G^- peaks are modified as $I_{G^+} \propto \cos^2(\theta_{\text{out}} + 3\phi)$ and $I_{G^-} \propto \sin^2(\theta_{\text{out}} + 3\phi)$, respectively. Figure 6b displays the intensity variations of the Raman peaks with the angle θ from a parallel to perpendicular orientation with respect to the strain axis in steps of 5° . In our case, our experimental data are analyzed and fitted to $I_{G^+} \propto \cos^2(\theta_{\text{out}} - 20^\circ)$ and $I_{G^-} \propto \sin^2(\theta_{\text{out}} - 20^\circ)$, which gives $\phi = -6.7^\circ$. We thus obtain the crystallographic orientation of graphene with respect to the strain axis. To manifest the band splitting and polarization dependence, the doubly degenerate G band is characterized with the angle θ' and modified as $\theta' = \theta - 20^\circ$. As shown in Figure 6c, the relative intensities of the G^+ and G^- peaks vary, which allows us to probe and demonstrate the crystallographic orientation of a certain sample.

3. Conclusion

In conclusion, rolling technology is proven to be a feasible approach for introducing uniaxial compressive strain in the graphene layer without a transfer process, which exhibits a strain-induced Raman band splitting, blueshift, and polarization

dependence. Based on the adopted elastic model in the tubular geometry, a compressive strain of $\approx 0.30\%$ is generated in graphene after the releasing and rolling process. Furthermore, by monitoring the mechanical behavior of an asymmetric tubular structure, all three Raman modes are related to the uniaxial strain with shift values of -17 ± 4.5 , -81 ± 7.9 , and $-156 \pm 17.7 \text{ cm}^{-1} \text{ \%}^{-1}$ for the G^+ , G^- , and 2D bands, respectively. Most strikingly, the Raman scattering of graphene is highly enhanced based on photon–phonon interactions, which arises from the strongly confined electromagnetic fields around the 3D tubular configuration. The observed polarization-dependent characteristics of the Raman scattering intensity arise from the anisotropic absorption of graphene, which match well with simulations. The synergy effect between the controllable strain engineering and enhanced interactions hints at an ideal method for novel graphene-integrated optical devices, e.g., lasers, sensors, photodetectors, and optical modulators.

Additionally, rolling technique offers a complete strain engineering capability for both the compressive and tensile cases. Compared with tensile cases, compression in graphene could induce out-of-plane deformation (buckling, crumpling, or rippling), which might strongly modify the mechanical and physical properties under a theoretical evaluation, thus making the phenomenon essential.^[61–63] The proposed technique could be applied for the fabrication of carbon nanotubes with controlled chiralities by rolling the graphene with different crystallographic orientations. Considering the fact that the optical and electronic properties of nanotubes significantly rely on their chirality, it is of great significance to elucidate and utilize the chiral preference for its untapped potential.^[64] In addition, since the 3D configuration could support optical resonances, the coupling between surface plasmons in graphene and photons in an optical device presents high potentials in “electron–photon” interaction research.^[65] Hence, our scheme enables new opportunities for the “phonon–electron–photon” process, providing the optical community with exciting prospects for physics and applications. Not just involving graphene, our approach is compatible with a variety of 2D materials, such as transition metal dichalcogenides, which builds a platform for precisely manipulating their intrinsic properties.^[66] Such a general concept of rolling technology promises new opportunities for studying the strain-related behaviors of graphene and other 2D materials, including photonic/electronic properties, thermal conductivity, and etc.

4. Experimental Section

Monolayer Graphene Preparation and Characterization: The large-area graphene on a $175 \mu\text{m}$ thick Ge (110) wafer (AXT) was fabricated by the CVD method. The Ge substrates were placed at the center of the

horizontal quartz tube, where the synthesis proceeded. The quartz tube was evacuated to 10^{-5} mbar and then filled with 200 standard cubic cm per min (sccm) argon (99.9999% purity) and 50 sccm hydrogen (99.9999% purity). After heating to the desired temperature (≈ 910 °C), 2.2 sccm methane (99.9999% purity) was introduced to deposit the graphene layer. After the deposition process of around 240 min, the monolayer graphene was obtained, then the methane gas was turned off and the furnace was cooled down to room temperature. The morphology of graphene was observed by AFM (Multimode 8, Bruker) in tapping mode. The XPS (PHI 5000, Perkin–Elmer) was carried out and the XPS spectra were fitted using a Gaussian-Lorentzian peak shape following Shirley background correction.

Microtube Fabrication: Based on the CVD-grown monolayer graphene, the strained oxide layers were directly deposited via electron beam evaporation (TSV70, Tenstar) under the following conditions: 25 °C ambient temperature and 10^{-6} mbar vacuum pressure. The Y_2O_3/ZrO_2 bilayer was chosen as the prestrained nanomembrane since the difference value of prestrain between the Y_2O_3 and ZrO_2 layer was sufficiently large. Additionally, the high refractive index of the Y_2O_3/ZrO_2 bilayer could enhance the evanescent field around the 3D construction and the coupling between the trilayer. A Y_2O_3 layer with a thickness of 10 nm was firstly deposited at a rate of 3.0 \AA s^{-1} , and a ZrO_2 layer with a thickness of 30 nm at the rate of 0.15 \AA s^{-1} . To transfer the designed patterns to the trilayer nanomembrane, a 1 \mu m photoresist of AZ-5214 (Microchemicals GmbH, Germany) was first spin coated and photolithographically patterned to an array of $150 \text{ \mu m} \times 150 \text{ \mu m}$ square under the following conditions: 5.6 s exposure time and 30 s develop time. Then, the patterned structure was etched via the ion beam etching (IBE, LKJ-3D-150, Advanced) process under the following conditions: 90 mA ion beam current, 500 eV ion energy, and 5.5 A main cathode current for 600 seconds. Subsequently, the uncovered trilayer would be etched away with the underlayer of Ge exposed. After dissolving the photoresist in alcohol, the sample was transferred to a heated (70 °C) and diluted (40% concentration) H_2O_2 (hydrogen peroxide) solution for etching the underlayer of Ge. Ge would then be selectively etched from the uncovered area, while the trilayer would be gradually released. After ≈ 20 min of the etching process, the patterned nanomembrane would be released and the microtube would be formed during the strain redistribution process. Finally, a critical point dryer (CPD 030, Leica) was applied, using liquid CO_2 (99.999% purity) as an intermedia to avoid the collapse of the fabricated 3D microstructure.

Micro-Raman Measurement: The Raman measurements were performed to characterize the behavior of rolled-up graphene at room temperature in an ambient atmosphere. An Ar^+ laser with an excitation wavelength of 514 nm was utilized as the pump source on a Raman spectroscope (HR800, Horiba). An excitation laser beam with a spot size of 1 \mu m (a 100X objective) was focused on the top surface of the resultant rolled-up structure. The output laser power was adjusted to 5 mW. The twice accumulation and 30 s integration time were fixed throughout all tests. The polarization characterization of the Raman feature was performed using a rotatable half-wave plate (AHWP05M-600, Thorlabs) and a fixed polarization analyzer (WP25M-VIS, Thorlabs).

Supporting Information

Supporting Information is available from the Wiley Online Library or from the author.

Acknowledgements

This work was supported by the Natural Science Foundation of China (51711540298, 61628401, and U1632115), the Science and Technology Commission of Shanghai Municipality (17JC1401700), the National Key Technologies R&D Program of China (2015ZX02102-003), the China Postdoctoral Science Foundation (No. KLH2021039), and the

Changjiang Young Scholars Program of China. S.L. acknowledges the financial support of the International Postdoctoral Exchange Fellowship Program (No. 20170010). Part of the experimental work was carried out in Fudan Nanofabrication Laboratory.

Conflict of Interest

The authors declare no conflict of interest.

Keywords

compressive strain, graphene, on-chip integration, photon–phonon interactions, rolling

Received: December 24, 2018

Revised: April 13, 2019

Published online: April 26, 2019

- [1] A. K. Geim, *Science* **2009**, *324*, 1530.
- [2] K. S. Novoselov, V. I. Fal'ko, L. Colombo, P. R. Gellert, M. G. Schwab, K. Kim, *Nature* **2012**, *490*, 192.
- [3] Y. Zhang, Y. Tan, H. L. Stormer, P. Kim, *Nature* **2005**, *438*, 201.
- [4] F. Schwierz, *Nat. Nanotechnol.* **2010**, *5*, 487.
- [5] A. A. Balandin, S. Ghosh, W. Bao, I. Calizo, D. Teweldebrhan, F. Miao, C. N. Lau, *Nano Lett.* **2008**, *8*, 902.
- [6] Y. Zhang, T. Tang, C. Girit, Z. Hao, M. C. Martin, A. Zettl, M. F. Crommie, Y. R. Shen, F. Wang, *Nature* **2009**, *459*, 820.
- [7] Y.-J. Yu, Y. Zhao, S. Ryu, L. E. Brus, K. S. Kim, P. Kim, *Nano Lett.* **2009**, *9*, 3430.
- [8] Z. H. Ni, T. Yu, Y. H. Lu, Y. Y. Wang, Y. P. Feng, Z. X. Shen, *ACS Nano* **2008**, *2*, 2301.
- [9] M. Huang, H. Yan, C. Chen, D. Song, T. F. Heinz, J. Hone, *Proc. Natl. Acad. Sci. USA* **2009**, *106*, 7304.
- [10] C. Si, Z. Sun, F. Liu, *Nanoscale* **2016**, *8*, 3207.
- [11] G. Gui, J. Li, J. Zhong, *Phys. Rev. B* **2008**, *78*, 075435.
- [12] F. Guinea, M. I. Katsnelson, A. K. Geim, *Nat. Phys.* **2010**, *6*, 30.
- [13] M. L. Teague, A. P. Lai, J. Velasco, C. R. Hughes, A. D. Beyer, M. W. Bockrath, C. N. Lau, N. C. Yeh, *Nano Lett.* **2009**, *9*, 2542.
- [14] G. W. Jones, D. A. Bahamon, A. H. Castro Neto, V. M. Pereira, *Nano Lett.* **2017**, *17*, 5304.
- [15] N. Levy, S. A. Burke, K. L. Meaker, M. Panlasigui, A. Zettl, F. Guinea, A. H. Castro Neto, M. F. Crommie, *Science* **2010**, *329*, 544.
- [16] C. T. Phare, Y.-H. D. Lee, J. Cardenas, M. Lipson, *Nat. Photonics* **2015**, *9*, 511.
- [17] X. Gan, R. Shiu, Y. Gao, I. Meric, T. F. Heinz, K. Shepard, J. Hone, S. Assefa, D. Englund, *Nat. Photonics* **2013**, *7*, 883.
- [18] I. Goykhman, U. Sassi, B. Desiatov, N. Mazurski, S. Milana, D. Fazio, A. Eiden, J. Khurgin, J. Shappir, U. Levy, A. C. Ferrari, *Nano Lett.* **2016**, *16*, 3005.
- [19] Q. Bao, H. Zhang, B. Wang, Z. Ni, C. H. Y. X. Lim, Y. Wang, D. Y. Tang, K. P. Loh, *Nat. Photonics* **2011**, *5*, 411.
- [20] T. M. G. Mohiuddin, A. Lombardo, R. R. Nair, A. Bonetti, G. Savini, R. Jalil, N. Bonini, D. M. Basko, C. Galiotis, N. Marzari, K. S. Novoselov, A. K. Geim, A. C. Ferrari, *Phys. Rev. B* **2009**, *79*, 205433.
- [21] G. Tsoukleri, J. Parthenios, K. Papagelis, R. Jalil, A. C. Ferrari, A. K. Geim, K. S. Novoselov, C. Galiotis, *Small* **2009**, *5*, 2397.
- [22] F. Ding, H. Ji, Y. Chen, A. Herklotz, K. Doerr, Y. F. Mei, A. Rastelli, O. G. Schmidt, *Nano Lett.* **2010**, *10*, 3453.
- [23] J. Zabel, R. R. Nair, A. Ott, T. Georgiou, A. K. Geim, K. S. Novoselov, C. Galiotis, *Nano Lett.* **2012**, *12*, 617.

- [24] Y. F. Mei, G. Huang, A. A. Solovev, E. B. Ureña, I. Mönch, F. Ding, T. Reindl, R. K. Y. Fu, P. K. Chu, O. G. Schmidt, *Adv. Mater.* **2008**, *20*, 4085.
- [25] Q. Guo, M. Zhang, Z. Xue, J. Zhang, G. Wang, D. Chen, Z. Mu, G. Huang, Y. F. Mei, Z. Di, X. Wang, *AIP Adv.* **2015**, *5*, 037115.
- [26] H. L. Zhen, G. S. Huang, S. Kiravittaya, S. L. Li, C. Deneke, D. J. Thurmer, Y. F. Mei, O. G. Schmidt, W. Lu, *Appl. Phys. Lett.* **2013**, *102*, 041109.
- [27] G. Huang, Y. F. Mei, *Adv. Mater.* **2012**, *24*, 2517.
- [28] I. D. Barcelos, L. A. B. Marçal, Ch. Deneke, L. G. Moura, R. G. Lacerda, A. Malachias, *RSC Adv.* **2016**, *6*, 103707.
- [29] G. Mao, Q. Wang, Z. Chai, H. Liu, K. Liu, X. Ren, *RSC Adv.* **2017**, *7*, 14481.
- [30] Y. Zhang, F. Liu, *Appl. Phys. Lett.* **2011**, *99*, 241908.
- [31] D. Chakravarty, C. S. Tiwary, L. D. Machado, G. Brunetto, S. Vinod, R. M. Yadav, D. S. Galvao, S. V. Joshi, G. Sundararajan, P. M. Ajayan, *Adv. Mater.* **2015**, *27*, 4534.
- [32] O. K. Park, C. S. Tiwary, Y. Yang, S. Bhowmick, S. Vinod, Q. Zhang, V. L. Colvin, S. Asif, R. Vajtai, E. S. Penev, B. I. Yakobson, P. M. Ajayan, *Nanoscale* **2017**, *9*, 6991.
- [33] V. Chabot, D. Higgins, A. Yu, X. Xiao, Z. Chen, J. Zhang, *Energy Environ. Sci.* **2014**, *7*, 1564.
- [34] D. Chakravarty, C. S. Tiwary, C. F. Woellner, S. Radhakrishnan, S. Vinod, S. Ozden, P. A. Da Silva Autreto, S. Bhowmick, S. Asif, S. A. Mani, D. S. Galvao, P. M. Ajayan, *Adv. Mater.* **2016**, *28*, 8959.
- [35] W. Gao, L. B. Alemany, L. Ci, P. M. Ajayan, *Nat. Chem.* **2009**, *1*, 403.
- [36] G. Huang, Y. F. Mei, *J. Mater. Chem. C* **2017**, *5*, 2758.
- [37] J. Zhang, J. Li, S. Tang, Y. Fang, J. Wang, G. Huang, R. Liu, L. Zheng, X. Cui, Y. F. Mei, *Sci. Rep.* **2015**, *5*, 15012.
- [38] B. Yao, C. Yu, Y. Wu, S.-W. Huang, H. Wu, Y. Gong, Y. Chen, Y. Li, C. W. Wong, X. Fan, Y. Rao, *Nano Lett.* **2017**, *17*, 4996.
- [39] W. Xi, C. K. Schmidt, S. Sanchez, D. H. Gracias, R. E. Carazo-Salas, R. Butler, N. Lawrence, S. P. Jackson, O. G. Schmidt, *ACS Nano* **2016**, *10*, 5835.
- [40] A. Madani, S. M. Harazim, V. A. Bolanos Quinones, M. Kleinert, A. Finn, E. S. G. Naz, L. Ma, O. G. Schmidt, *Opt. Lett.* **2017**, *42*, 486.
- [41] Y. Li, Y. Fang, J. Wang, L. Wang, S. Tang, C. Jiang, L. Zheng, Y. F. Mei, *Lab Chip* **2016**, *16*, 4406.
- [42] J. Wang, T. Zhan, G. Huang, P. K. Chu, Y. F. Mei, *Laser Photonics Rev.* **2014**, *8*, 521.
- [43] S. Li, L. Ma, H. Zhen, M. R. Jorgensen, S. Kiravittaya, O. G. Schmidt, *Appl. Phys. Lett.* **2012**, *101*, 231106.
- [44] H. Wang, H. Zhen, S. Li, Y. Jing, G. Huang, Y. F. Mei, W. Lu, *Sci. Adv.* **2016**, *2*, e1600027.
- [45] Z. Tian, B. Xu, B. Hsu, L. Stan, Z. Yang, Y. F. Mei, *Nano Lett.* **2018**, *18*, 3017.
- [46] B. Xu, Z. Tian, J. Wang, H. Han, T. Lee, Y. F. Mei, *Sci. Adv.* **2018**, *4*, eaap8203.
- [47] B. Xu, B. Zhang, L. Wang, G. Huang, Y. F. Mei, *Adv. Funct. Mater.* **2018**, *28*, 1705872.
- [48] G. Wang, M. Zhang, Y. Zhu, G. Ding, D. Jiang, Q. Guo, S. Liu, X. Xie, P. K. Chu, Z. Di, X. Wang, *Sci. Rep.* **2013**, *3*, 2465.
- [49] X. Zheng, L. Gao, Q. Yao, Q. Li, M. Zhang, X. Xie, S. Qiao, G. Wang, T. Ma, Z. Di, J. Luo, X. Wang, *Nat. Commun.* **2016**, *7*, 13204.
- [50] J.-H. Lee, E. K. Lee, W.-J. Joo, Y. Jang, B.-S. Kim, J. Y. Lim, S.-H. Choi, S. J. Ahn, J. R. Ahn, M.-H. Park, C.-W. Yang, B. L. Choi, S.-W. Hwang, D. Whang, *Science* **2014**, *344*, 286.
- [51] J. Dai, D. Wang, M. Zhang, T. Niu, A. Li, M. Ye, S. Qiao, G. Ding, X. Xie, Y. Wang, P. K. Chu, Q. Yuan, Z. Di, X. Wang, F. Ding, B. I. Yakobson, *Nano Lett.* **2016**, *16*, 3160.
- [52] J. Sha, Y. Li, R. Villegas Salvatierra, T. Wang, P. Dong, Y. Ji, S. Lee, C. Zhang, J. Zhang, R. H. Smith, P. M. Ajayan, J. Lou, N. Zhao, J. M. Tour, *ACS Nano* **2017**, *11*, 6860.
- [53] J. Wang, T. Zhan, G. Huang, X. Cui, X. Hu, Y. F. Mei, *Opt. Express* **2012**, *20*, 18555.
- [54] A. C. Ferrari, D. M. Basko, *Nat. Nanotechnol.* **2013**, *8*, 235.
- [55] X. Lin, Y. Fang, L. Zhu, J. Zhang, G. Huang, J. Wang, Y. F. Mei, *Adv. Opt. Mater.* **2016**, *4*, 936.
- [56] I. D. Barcelos, L. G. Moura, R. G. Lacerda, A. Malachias, *Nano Lett.* **2014**, *14*, 3919.
- [57] G. P. Nikishkov, *J. Appl. Phys.* **2003**, *94*, 5333.
- [58] M. Grundmann, *Appl. Phys. Lett.* **2003**, *83*, 2444.
- [59] V. M. Pereira, A. H. C. Neto, *Phys. Rev. Lett.* **2009**, *103*, 046801.
- [60] G. Gui, D. Morgan, J. Booske, J. Zhong, Z. Ma, *Appl. Phys. Lett.* **2015**, *106*, 053113.
- [61] J. A. Baimova, B. Liu, S. V. Dmitriev, K. Zhou, *J. Phys. D: Appl. Phys.* **2015**, *48*, 095302.
- [62] S. C. Pradhan, T. Murmu, *Comput. Mater. Sci.* **2009**, *47*, 268.
- [63] C. Chen, W. Bao, J. Theiss, C. Dames, C. N. Lau, S. B. Cronin, *Nano Lett.* **2009**, *9*, 4172.
- [64] N. Pierce, G. Chen, L. P. Rajukumar, N. H. Chou, A. L. Koh, R. Sinclair, S. Maruyama, M. Terrones, A. R. Harutyunyan, *ACS Nano* **2017**, *11*, 9941.
- [65] B. Yao, S.-W. Huang, Y. Liu, A. K. Vinod, C. Choi, M. Hoff, Y. Li, M. Yu, Z. Feng, D.-L. Kwong, Y. Huang, Y. Rao, X. Duan, C. W. Wong, *Nature* **2018**, *558*, 410.
- [66] F. Xia, H. Wang, D. Xiao, M. Dubey, A. Ramasubramaniam, *Nat. Photonics* **2014**, *8*, 899.